B-type olivine fabrics developed in the fore-arc side of the mantle wedge along a subducting slab

Miki Tasaka[a], Katsuyoshi Michibayashi[b] *, David Mainprice[c]

[a]*Department of Earth and Planetary Science, The University of Tokyo, Tokyo 113-0033, Japan*

[b]*Institute of Geosciences, Shizuoka University, Shizuoka 422-8529, Japan*

[c]*Géosciences Montpellier, UMR 5243 CNRS/Université Montpellier II, Montpellier, France*

* Corresponding author. *Institute of Geosciences, Shizuoka University, Shizuoka 422-8529, Japan*. Tel.:+81 54 238 4788 ; fax:+81 54 238 0491.

E-mail address: sekmich@ipc.shizuoka.ac.jp

Re-submitted to Earth and Planetary Sciences Letters 15th May 2008

Abstract

B-type olivine fabrics are pervasive within highly depleted dunites of the small-sized Imono peridotite body located within the subduction-type Sanbagawa metamorphic belt of the southwest Japan arc. The dunites contain various microstructures, ranging from porphyroclastic to fine-grained intensely sheared textures. The Mg/(Mg + Fe) atomic ratios (Fo number) of olivine within these dunites are consistently around 0.9, as are the Cr/(Cr + Al) atomic ratios (Cr number) of chromian spinel, suggesting their evolution from a highly depleted magma (boninite). These data provide strong thermal constraints on the formation of the highly depleted dunites, as their formation requires hot, hydrous, shallow mantle (>1250 °C at <30 km depth) in the mantle wedge. Because the Sanbagawa metamorphic belt finally entrained these peridotites during progressive retrogression, B-type olivine fabrics probably developed in the fore-arc side of the subduction zone, above or along the subducting slab, possibly in association with dehydration fluids derived from the slab. The previously documented small magnitude of S-wave splitting can be explained by the seismic properties of B-type peridotites within an anisotropic layer of approximately several kilometers in thickness, oriented by flow parallel to the subducting slab, under maximum temperatures of 880–1030 °C depending on the flow stress. These findings indicate that such a B-type layer could constitute a dominant source of seismic S- and P-wave anisotropy in mantle wedge regions.

Key words: B-type olivine fabric, dunite, mantle wedge, hydration, subduction, seismic anisotropy

1. Introduction

Water is pervasive in mantle wedges due to extensive dehydration of the underlying subducting slab (e.g., Tatsumi, 1989; Hacker et al., 2003; Stockhert and Gerya, 2005). The mantle wedge is therefore one of the mostly likely sites where water influences the development of olivine fabrics. Indeed, olivine fabrics characterized by an a-axis maximum oriented perpendicular to the flow direction (B-type fabric; Jung and Karato, 2001a; Katayama and Karato, 2006; Jung et al., 2006) are thought to develop in the mantle wedge under conditions of high water activity and high stress (Karato, 1995, 2003). There is growing interest in the role of olivine fabrics in the mantle-wedge part of fore-arc mantle, where the maximum seismic-wave velocity is oriented normal to the direction of plastic flow in the upper mantle (Audoine et al., 2004; Nakajima and Hasegawa, 2004; Kneller et al., 2005, 2007, 2008; Lassak et al., 2006; Conder and Wiens, 2007; Long et al., 2007), yet only a handful of natural examples of such fabrics have been briefly reported (e.g., Mizukami et al., 2004; Skemer et al., 2006).

B-type olivine fabrics have been described from peridotites of the Higashi-Akaishi peridotite body of the Sanbagawa metamorphic belt in southwest Japan (Mizukami et al., 2004); however, such fabrics only occur within olivine with fine-grained texture; typical coarse granular peridotites possess the more common A-type fabrics that develop under anhydrous conditions at high-temperature and low stress (Mizukami et al., 2004; Mizukami and Wallis, 2005). Therefore, the rare occurrence of B-type fabrics indicates that they are not the dominant fabric of the fore-arc region.

In the present paper, we present new examples of B-type fabrics within a small peridotite body located close to the Higashi-Akaishi body. B-type fabrics not only occur within peridotite with porphyroclastic to fine-grained equigranular texture, but also within dunites that possibly evolved from highly depleted magma. In our discussion, we compare the seismic properties of the B-type olivine fabrics with measured seismic anisotropy in the fore-arc region of the mantle wedge. Our findings indicate that B-type fabrics explain the phenomenon of fast trench-parallel S-wave polarization and fast trench-normal P-waves.

2. Geological setting and sample description

The Sanbagawa belt of southwest Japan (Fig. 1A) is one of the world's best-documented examples of a subduction-type high-pressure/temperature metamorphic

body. The following brief outline of the geological setting of the study area is largely after Mizukami and Wallis (2005). The Sanbagawa belt represents the deeper parts of a strongly deformed accretionary complex that formed during the Cretaceous subduction of oceanic lithosphere at the Eurasian continental margin (e.g., Banno et al., 1986; Takasu and Dallmeyer, 1990; Wallis, 1998; Okamoto et al., 2000). The highest-grade part of the Sanbagawa belt is exposed in the Besshi area, central Shikoku (Fig. 1A), where it is divided into the Besshi unit and a series of high pressure (HP) bodies that record eclogite facies metamorphism (Kunugiza et al., 1986; Takasu, 1989). The Besshi unit consists mainly of pelitic, basic and siliceous schists. Peak metamorphic conditions are generally of the greenschist to epidote-amphibolite facies, and the unit is divided into chlorite, garnet, albite-biotite and oligoclase-biotite zones based on the mineralogy of metapelites (Fig. 1A; Banno et al., 1978; Enami, 1982; Higashino, 1990). The metamorphic history of the Besshi unit is characterized by a series of clockwise $\underline{P}$–$\underline{T}$ paths involving an increase in temperature subsequent to peak metamorphic pressure (0.6–1.1 GPa; Enami et al., 1994; Aoya, 2001). The HP eclogite bodies consist mainly of mafic and ultramafic lithologies. The mafic rocks are schistose or consist of massive garnet-bearing epidote amphibolite with local relic eclogite. These bodies are distinguished from the Besshi unit by significantly higher peak metamorphic pressures, above 1.5 GPa (e.g., Takasu, 1989; Wallis et al., 2000), and the fact that they structurally overlie the unit (Wallis and Aoya, 2000; Aoya, 2002).

The most intensely studied ultramafic body in the Sanbagawa belt is the Higashi-Akaishi peridotite body, which consists mainly of dunite and intercalated layers of wehrlite, clinopyroxenite, chromitite, and minor garnet-bearing rocks (Horikoshi, 1937; Yoshino, 1961, 1964; Mori and Banno, 1973; Enami et al., 2004; Mizukami et al., 2004; Mizukami and Wallis, 2005). Thermobarometric analyses of the garnet-bearing rocks indicate ultra-high pressure (UHP) conditions above 3 GPa (Enami et al., 2004).

The small Imono peridotite body is located 5 km to the east of Mt. Higashi-Akaishi (Fig. 1A) and has a rectangular surface outcrop over an area of 300 × 400 m^2 (Fig. 1B). The Imono body is dominantly dunite (Kunugiza et al., 1984). The dunite is serpentinized in places, presumably related to exhumation; however, the earlier olivine-rich microstructures and associated petrological information are well preserved in some outcrops. We collected 37 oriented samples from the eastern side of the Imono peridotite body at a large outcrop that extends over 100 m section (N08 in Fig. 1B). The

aligned spinel grains define foliation plane (XY) and lineation (X) within the sample, X, Y and Z are the axes of the orthogonal structural reference frame we will use to describe the sample orientation. We observed these structures on bleached and saw-cut samples in the laboratory. The foliation generally strikes WNW–SSE and dips moderately to the NNE; the mineral lineation plunges to the north (Fig. 1B). The orientations of the foliation and lineation are consistent with those measured in the Higashi-Akaishi peridotite body (Yamamoto et al., 2004).

3. Microstructural analyses

We analysed microstructures in all samples using thin sections cut perpendicular to the foliation (Z) and parallel to the lineation (X) (i.e., XZ-sections). Because the Imono peridotite body is dominated by dunite, the samples consist mainly of olivine and a small amount of spinel, with various degrees of serpentinization. For further analyses, we selected 5 of the 37 samples that showed the best-preserved peridotite microstructures. The complete set of samples will be described elsewhere.

Among the five analysed samples, four contain porphyroclastic texture with fine-grained (~0.05 mm) neoblasts (Fig. 2A–D). Porphyroclasts are 1–3 mm in size, which have intense undulose extinction, kinking, and the development of sub-grain boundaries. The porphyroclasts tend to become smaller with increasing proportion of neoblasts (Fig. 2A–D). The aspect ratios of the porphyroclasts are generally around 2. One sample (N08H-2) is cut by a thin, fine-grained (~0.05 mm) equigranular layer (Fig. 2E). Sample N08Ha consists entirely of a fine-grained equigranular texture (Fig. 2F), with relatively straight grain boundaries that meet at triple junctions.

The sizes of olivine grains were measured in each sample, and the outlines of approximately 200 olivine grains were carefully traced from photomicrographs. The area (A) of each grain was then measured using Scion Image software. Grain size (D) was calculated as $D = 2(A/3.14)^{0.5}$ (e.g., Michibayashi and Masuda, 1993; Okamoto and Michibayashi, 2005), representing the diameter of a circle with the same area as that of the grain. The average grain sizes for the samples analyzed in this study vary between 30 and 400 μm (Supplementary Table 1).

4. Textural analyses

We measured the crystal-preferred orientations (CPOs) of olivine grains from

highly polished thin sections using a scanning electron microscope equipped with an electron-backscatter diffraction system (JEOL JSM6300 with HKL Channel5), housed at the Centre for Instrumental Analysis, Shizuoka University, Japan. We measured between 196 and 384 olivine crystal orientations per sample (Fig. 3), visually confirming the computerized indexation of the diffraction pattern for each orientation. The measured olivine CPOs are presented on equal area, lower hemisphere projections in the structural (XZ) reference frame (Fig. 3). To characterize the CPOs, we determined the fabric strength and distribution density of the principal crystallographic axes (for the *J* index and *pfJ* index, see Mainprice et al., 2000; Michibayashi and Mainprice, 2004; Michibayashi et al., 2006a; for the *M* index, see Skemer et al., 2006).

All of the analysed samples show a distinct alignment of [001] axes parallel to the lineation (X), [010] axes normal to the foliation (Z), and [100] axes normal to the lineation and within the plane of the foliation (Y): i.e., a [001] (010) CPO pattern (Fig. 3). The fabric strength varies from J=2.59 to 5.33 (M=0.037 to 0.190) within the porphyroclastic textures (Fig. 3A-D). For sample N08H-1, we separately analysed the CPOs of porphyroclasts and neoblasts. The two sets of grains show similar CPO patterns, although with different degrees of fabric intensity (C1 and C2 in Fig. 3; porphyroclasts, J=9.16 (M=0.239); neoblasts, J=5.39 (M=0.184)). For two samples with fine-grained equigranular texture, one shows an intense [001] (010) pattern (Fig. 3E) and the other shows girdles of [100] and [001] about the foliation (XY plane) and an intense alignment of [010] normal to the foliation (Z) (Fig. 3F). The fabric strengths of the fine-grained texture are relatively high: J=6.07 to 7.12 (M=0.140 to 0.191).

The fabric intensities determined for all samples are listed in Supplementary Table 1. The *J*-index values range from 2.59 to 7.12, less than those determined in similar rocks elsewhere such the Oman ophiolite (Michibayashi and Mainprice, 2004; Michibayashi et al., 2006a) and peridotite xenoliths from northeast Japan (Michibayashi et al., 2006b). The trends of the pole figure index *pfJ* generally follow the trends of the *J*-index, with [010] *pfJ* being typically the strongest, [001] *pfJ* intermediate, and [100] *pfJ* the weakest among the three axes (Fig. 3; Supplementary Table 1).

5. Mineral chemistry

The chemical compositions of olivine and chromium spinel within the five samples shown in Fig. 2 were analysed using a JEOL electron microprobe (JXA733)

175 housed at the Centre for Instrumental Analysis, Shizuoka University, Japan. Analytical
176 conditions were 15 kV accelerating voltage and 12 nA probe current. Special care was
177 taken in analysing the MnO and NiO contents of olivine, using a long count time of 30 s
178 compared with 10 s for the other elements. Ferrous and ferric iron contents of chromian
179 spinel were calculated assuming spinel stoichiometry. The Cr number was calculated as
180 the Cr/(Cr + Al) atomic ratio of chromian spinel. The Mg number was calculated as the
181 Mg/(Mg + total Fe) atomic ratio for silicates and Mg/(Mg + Fe^{2+}) atomic ratio for
182 chromian spinel.
183 The analysed minerals were largely homogeneous in chemistry (representative
184 analyses are listed in Supplementary Table 2). The peridotites plot within the
185 olivine-spinel mantle array (OSMA; Fig. 4A), which represents a spinel peridotite restite
186 trend for olivine and chromian spinel (Arai, 1987, 1994a). The olivine composition is
187 Fo_{90-92}, and the Cr number of spinel ranges from 0.80 to 0.98 (Fig. 4A). NiO_2
188 concentration tends to decrease slightly with decreasing Mg number of olivine, similar to
189 the fractional crystallization trend of Takahashi (1987; Fig. 4B). The TiO_2 content is
190 remarkably constant within all different microstructures, being less than 0.2 wt% (Fig.
191 4C).
192
193 **6. Rock seismic anisotropy**
194 *6.1. Rock seismic properties*
195 The seismic properties of a rock mass can be computed by averaging the elastic
196 constants of the individual grains in their orientation in the sample reference frame
197 (X,Y,Z) for each mineral and weighting their contribution using the modal composition of
198 the aggregate (Mainprice et al., 2000). Given that all of the samples in the present study
199 are dunites, we calculated the seismic properties assuming a composition of 100% olivine
200 (Fig. 5). The elastic constants of olivine used for the calculations are from Abramson et al.
201 (1997), at ambient conditions, and we used the Voigt-Reuss-Hill averaging scheme
202 (Mainprice et al., 2000). The P-wave anisotropy was calculated as a percentage using the
203 formula $200(Vp_{max} - Vp_{min})(Vp_{max} + Vp_{min})$, and the S-wave anisotropy (AVs) was
204 calculated for a specific propagation direction using the formula $200(Vs_1 - Vs_2)/(Vs_1 +$
205 $Vs_2)$, where Vs_1 and Vs_2 are the fast and slow wave velocities, respectively (e.g., Pera et
206 al., 2003).
207 The seismic velocities (Vp, Vs_1, Vs_2) and seismic anisotropy determined for

each sample are listed in Supplementary Table 3. All of the calculated seismic velocities are similar among the samples, with little variability observed. Values of Vp_{max} range from 8.51 to 8.77 km/s (Vp_{mean}=8.77 km/s), Vs_{1max} from 4.89 to 5.00 km/s (Vs_{1mean}=4.93 km/s), and Vs_{2max} from 4.81 to 4.86 km/s (Vs_{2mean}=4.85 km/s). Seismic anisotropy shows greater variation: AVp ranges from 4.50 to 9.80% (AVp_{mean}=5.45%) and AVs from 3.16 to 6.96% (AVs_{mean}=4.00%).

Figure 5 shows stereographic projections of Vp and AVs and the orientation of the polarization plane of the fastest Vs (Vs_1). For all microstructure types, Vp is fastest normal to the lineation, within the plane of the foliation (Y) (Fig. 5). This orientation is directly related to the CPO maximum of olivine [100] (Fig. 3), the fastest direction within the olivine crystal. Vp is lowest normal to the foliation (Z), whereas the intermediate direction tends to be subparallel to the lineation (X) (Fig. 5). Only one sample deviates from this trend: in N08Ha, Vp is fastest parallel to the lineation and defines a girdle within the plane of the foliation (XY); the slowest direction is normal to the foliation (Z) (Fig. 5F).

The variation in polarization anisotropies (AVs) among the samples possibly reflects variations in orientation distributions and intensities (compare Figs. 3 and 5). The orientation of the polarization plane of Vs_1 marks the orientation of the great circle that contains the maximum concentration of [100]. Accordingly, because [100] tends to be aligned normal to the lineation and within the plane of the foliation (Y) (Fig. 3), the orientation of the polarization plane of Vs_1 parallel to the Z-axis is normal to the lineation (X) (Fig. 5).

6.2. Variation in seismic properties as a function of P and T

To test for any correlation between the petrophysical and geophysical data, we calculated the seismic properties over a large range of pressure (0.5–5 GPa) and temperature (600–1400 °C) according to the method described by Mainprice et al. (2000) and Mainprice (2007). We used a calculated average sample by summing all of the data in Fig. 3 (see Fig. 6A).

To calculate the elastic constants at various pressures and temperatures, the single-crystal elastic constants are given at the pressure and temperature of measurement using the following relationship:

$$C_{ij}(PT) = C_{ij}(P_0T_0) + (dC_{ij}/dP)(P-P_0) + 1/2(d^2C_{ij}/dP^2)(P-P_0)^2 + (dC_{ij}/dT)(T-T_0)$$

$+ (d^2C_{ij}/dPdT)(P-P_0)(T-T_0)$,

where $C_{ij}(PT)$ is the elastic constant at pressure P and temperature T, $C_{ij}(P_0T_0)$ is the elastic constant at a reference pressure P_0 (e.g., 0.1 MPa) and temperature T_0 (e.g., 25 °C), dC_{ij}/dP is the first-order pressure derivative, dC_{ij}/dT is the first-order temperature derivative, and d^2C_{ij}/dP^2 is the second-order pressure derivative (see Mainprice, 2007).

The seismic velocities also depend on the density of the minerals at a given pressure and temperature; this can be calculated using an appropriate equation of state (Knittle, 1995). The Murnaghan equation of state, derived from finite strain, is sufficiently accurate at moderate compression (Knittle, 1995) of the upper mantle, yielding the following expression for density as a function of pressure:

$$\rho(P) = \rho_0(1+(K'/K).(P-P_0))1/K'$$

where K is the bulk modulus; $K' = dK/dP$, the pressure derivative of K; and ρ_0 is the density at reference pressure P_0 and temperature T_0. With changing temperature, the density varies as follows:

$$\rho(T) = \rho_0[1-\int\alpha_v(T)dT] \approx \rho_0[1 - \alpha_{av}(T-T_0)]$$

where $\alpha_v(T) = 1/V(\partial V/\partial T)$ is the volume thermal expansion coefficient as a function of temperature and α_{av} is an average value of thermal expansion that is constant over the temperature range (Fei, 1995). For the temperatures and pressures of the mantle, the density is described in this paper as follows:

$$\rho(P,T) = \rho_0\{(1+(K'/K).(P-P_0))1/K'[1 - \alpha_{av}(T-T_0)]\}.$$

We employed the elastic constants of Abramson et al. (1997) for olivine Fo_{90} and the first- and second-order pressure derivatives by the same authors, and first-order temperature derivatives of Issak (1992). The elastic constants of the resulting rocks are presented in Supplementary Table 4, and a set of seismic anisotropies calculated at 800°C and 2.8 GPa (using the Voigt–Reuss–Hill average for the average sample shown in Fig. 6A) is shown in Fig. 6B.

We calculated variations in the seismic properties as a function of pressure and temperature for the structural plane XY for a horizontal shear (Fig. 7A), XZ for a lateral shear (Fig. 7B), YZ for a vertical shear (Fig. 7C), and a titled slab for a shear along the slab (Fig. 7D). We chose these orientations because they correspond to different orientations of corner flow in the mantle wedge (Fig. 7E). The amount of slab tilt in Fig. 7D was taken to be 30° for the northeast Japan arc (e.g., Hasegawa et al., 1978), because the Imono peridotites developed in the mantle wedge during the Cretaceous subduction of

oceanic lithosphere of the Pacific plate at the Eurasian continental margin. The tectonic setting for the Imono peridotites might have been similar to that of the northeast Japan arc rather than the southwest Japan arc, where young, hot oceanic lithosphere of the Philippine Sea plate is currently being subducted (e.g., Maruyama et al., 1997). We chose to consider the following typical propagation directions of seismic waves: vertical propagation for S-waves and propagation in the horizontal plane for P-waves (Fig. 7E).

Figure 8 shows variations in the average Vp and deviation of Vp as a function of pressure and temperature for the orientation of structural planes shown in Fig. 7, as well as the S-wave anisotropy for various propagation directions. The dotted triangles in Fig. 8 represent the possible *PT* conditions for B-type olivine fabrics of the Imono peridotite body, as discussed below. Among the three investigated seismic parameters, Vp is the most sensitive to variations in *PT* in all structural orientations: the deviation of Vp and the S-wave anisotropy show considerably less variation (Fig. 8).

7. Discussion

7.1. B-type olivine fabrics within various microstructures

The olivine CPO patterns presented in Fig. 3 show that B-type fabrics occurs throughout the Imono peridotite body, in association with both porphyroclastic and fine-grained equigranular textures (compare Figs. 2 and 3). In samples with porphyroclastic texture, the grain sizes of neoblasts are relatively similar to those in samples with fine-grained equigranular texture (i.e., ~0.05 mm), suggesting that the latter texture arose from the complete dynamic recrystallization of porphyroclastic texture. This interpretation is further supported by the fact that a thin layer of fine-grained equigranular texture (Fig. 2E) cuts across an area of porphyroclastic texture (Fig. 2C). We therefore conclude that the porphyroclastic textures observed within the Imono peridotite body resulted from various degrees of dynamic recrystallization, presumably of the primarily coarser granular texture. Furthermore, because the porphyroclastic texture can be divided into two domains, porphyroclasts and neoblasts, we confirmed that both domains have the same B-type olivine fabrics (e.g., Fig. 3C1 for porphyroclasts and 3C2 for neoblasts, respectively). We therefore interpret that the B-type olivine fabrics could have developed at an early stage associated with coarser granular texture within the Imono peridotite body and maintained their character, with increasing shearing, during grain size reduction by dynamic recrystallization.

Grain size is expected to change until recrystallized grains attain a steady-state size, as determined by the flow stress (Twiss, 1977; Michibayashi, 1993). If we assume that the mean grain size in the fine-grained equigranular texture represents a steady-state grain size, we can then use grain size as a paleopiezometer to infer flow stress (e.g., van der Wal et al., 1993; Jung and Karato, 2001b). The two samples with fine-grained equigranular texture have mean grain sizes of 33 and 95 μm (Supplementary Table 1). Therefore, the inferred flow stresses for the B-type fabrics would be 100 and 200 MPa for wet olivine or 40 and 100 MPa for dry olivine, respectively, based on the relationship between grain size and stress shown by Jung and Karato (2001b).

7.2. Petrological constraints on the origin of the Imono peridotite body

The Imono peridotite consists solely of dunite with accessory spinel, placing it in the spinel peridotite facies, which is stable in the low-pressure (<1.5 GPa) regions of the mantle. All of the samples collected from the Imono peridotite body contain spinel with high Cr numbers (0.98–0.80) and olivine with high Mg numbers (0.90–0.92) (Fig. 4A). These rocks are highly depleted compared with abyssal peridotites and fore-arc peridotites, which commonly contain spinels with lower Cr numbers (<0.6) (e.g., Arai, 1994a). Moreover, the relationship between NiO_2 content and the Mg number of olivine shows a fractional crystallization trend (Fig. 4B). It is therefore likely that the dunites from the Imono peridotite body formed after a high degree of partial melting, presumably fluxed by a supply of water, to produce refractory melts that potentially precipitated spinels with high Cr numbers (Takahashi et al., 1987; Kelemen, 1990; Arai, 1992, 1994b). It is also important to note that the TiO_2 content of the spinel analysed in the present study is consistently less than 0.2 wt%. Spinel with a high Cr number and low Ti content is characteristic of arc magma such as high-Mg arc basalt or boninite (Fig. 4A and C; Arai, 1992). According to the experimental study of Umino and Kushiro (1989), the pressure and temperature conditions required for the formation of boninitic melt are 0.3–0.8 GPa and >1250 °C, respectively.

7.3. Tectonic evolution of the Imono peridotite body within the mantle wedge

The Imono peridotite body is one of a number of ultramafic lithologies, along with the Higashi-Akaishi peridotite body, entrained in the subduction-type Sanbagawa metamorphic belt. B-type olivine fabrics have also been reported from the nearby

Higashi-Akaishi peridotite body (Mizukami et al., 2004; Fig. 1A); however, in contrast to the olivine fabrics in the Imono peridotite body, B-type fabrics in the Higashi-Akaishi body have only been found within olivine neoblasts: whereas olivine porphyroclasts appear to have A-type fabrics (Mizukami et al., 2004). B-type olivine fabrics of the Higashi-Akaishi peridotite body are thought to be part of the D_{2B} deformation stage, during which time strong planar and linear structures formed, subsequently developing into an antigorite-defined schistosity (Mizukami and Wallis, 2005). Such an antigorite schistosity is also found within the fine-grained texture of the Imono peridotite body (Fig. 2), raising the possibility that the exhumation history of the Imono peridotite body is similar to that of the Higashi-Akaishi peridotite body.

The peak of metamorphic pressure recorded within the Sanbagawa belt is 0.6–1.1 GPa (Fig. 9; Enami et al., 1994; Aoya, 2001). The Higashi-Akaishi peridotite body experienced pressures as high as 3 GPa during the D_2, and after D_3 it was amalgamated with the Besshi unit at a pressure of around 1 GPa (Mizukami and Wallis, 2005). The D_2 stage in the Higashi-Akaishi peridotite body is characterized by an approximately isothermal burial path at temperatures of 750–800 °C, reaching UHP conditions (above 2.8 GPa; D_{2A} in Fig. 9); this path could be explained by the evolution of the Higashi-Akaishi peridotite body in the Sanbagawa subduction zone (Mizukami and Wallis, 2005). Furthermore, high water activity during D_2 is indicated by micro-inclusions in dusty olivine porphyroclasts (Mizukami et al., 2004). Prograde metamorphic changes in the subducting slab are characterized by dehydration reactions that could account for the introduction of water to the peridotite body during D_2 (Mizukami and Wallis, 2005); therefore, the B-type olivine fabrics in the Higashi-Akaishi peridotite body developed under high water activity during D_2 (Fig. 9; Mizukami et al., 2004).

The dunites within the Imono peridotite are highly depleted cumulates, possibly derived from boninitic melt that formed at shallow depths (<0.8 GPa; i.e., ca. <30 km) and high temperature (>1250 °C; Umino and Kushiro, 1989). This provides strong thermal constraints on the formation of the Imono peridotite body, which requires hot, hydrous, shallow mantle; in contrast, the Higashi-Akaishi peridotite body requires cold, hydrous, deep mantle along the subducting slab (Fig. 9). Whereas petrological and microstructural data from the Higashi-Akaishi peridotite body can be used to constraint its *P-T* path prior to incorporation within the Sanbagawa metamorphic rocks, no such

373 constraints exist for the Imono peridotite body, except for its boninitic association.
374 For depleted dunites that formed at such high temperatures, their deformation
375 fabrics would be A- or C-type, depending on the amount of available water (Katayama
376 and Karato, 2006). Therefore, a B-type fabric should have formed as the rock mass cooled.
377 Katayama and Karato (2006) presented an olivine fabric diagram in temperature–stress
378 space at constant pressure (2.0 GPa) under water-saturated conditions. As discussed
379 above, the inferred stress for the B-type fabrics analyzed in this study lies in the range
380 100–200 MPa for wet olivine. Based on the olivine fabric diagrams of Katayama and
381 Karato (2006), these stress estimates indicate maximum temperatures for the B-type
382 fabrics of approximately 880–1030 °C, depending on the flow stress estimated from the
383 mean sizes of dynamically recrystallized grains (Fig. 9).
384 As described above, the antigorite schistosity within the fine-grained texture in
385 the Imono peridotite body is similar to that in the Higashi-Akaishi peridotite body.
386 Therefore, after the formation of the Imono peridotite body at a relatively shallow depth
387 (<0.8 GPa), the Imono peridotite body might have been entrained by the Sanbagawa belt
388 at a pressure of around 1 GPa, following a similar high-pressure path to that of the
389 Higashi-Akaishi peridotite body (Fig. 9). Alternatively, given that the initial pressure
390 conditions experienced by the Imono body (<0.8 GPa) were markedly different from
391 those of the Higashi-Akaishi peridotite body (~3 GPa), its *P*-*T* path may be different from
392 that for the Higashi-Akaishi body. Thus, the Imono peridotite body may have been
393 displaced slightly downward to attain pressures equivalent to those of the peak
394 metamorphic pressure in the Sanbagawa belt during cooling (Fig. 9). Nonetheless, the
395 Imono peridotite body is likely to have been located in the fore-arc mantle wedge along a
396 subducting slab (i.e., an active subduction zone), along with the Higashi-Akaishi
397 peridotite body (Mizukami and Wallis, 2005).
398
399 *7.4. Implications for seismic anisotropy measurements*
400 It is generally accepted that anisotropy in the back-arc area is likely to reflect
401 olivine fabrics in the mantle. In contrast, several possible causes of anisotropy in the
402 fore-arc side have been considered: deformation of water-rich olivine (i.e., B-type
403 fabrics) in the mantle wedge (Jung and Karato, 2001a; Audoine et al., 2004; Katayama
404 and Karato, 2004, 2006; Kneller et al., 2005, 2007, 2008; Jung et al., 2006),
405 trench-parallel flow in the mantle wedge arising from along-strike variations in the dip of

406 the slab (e.g., Smith et al., 2001; Peyton et al., 2001; Conder and Wien, 2007, Kneller and
407 van Keken, 2007; Behn et al., 2007), anisotropy in the crust and slab (e.g., Currie et al.,
408 2001; Ishise and Oda, 2005), and the occurrence of highly anisotropic foliated antigorite
409 serpentine (e.g., Kneller et al., 2008).
410 Although we are unable to determine which of these factors is dominant in the
411 fore-arc side of the mantle wedge, we confirmed the presence of B-type olivine fabrics
412 along a subducting slab. The Sanbagawa belt, within which the Imono peridotite body
413 occurs, is thought to have formed during Cretaceous subduction at the Eurasian
414 continental margin (e.g., Maruyama et al., 1997). The northeast Japan arc appears to be an
415 ideal mantle wedge, as the cold Pacific plate subducts beneath the Eurasian plate at a rate
416 of ~10 cm/year (e.g., Maruyama et al., 1997). The seismology of the northeast Japan arc
417 has been intensively studied, including shear-wave polarization (Nakajima and Hasegawa,
418 2004) and P-wave anisotropy (Ishise and Oda, 2005). Fast S-wave directions in the
419 back-arc side are oriented approximately E–W, whereas those in the fore-arc side are
420 oriented approximately N–S, suggesting contrasting patterns of anisotropy in the
421 back-arc and fore-arc areas (Nakajima and Hasegawa, 2004). Therefore, we now evaluate
422 the influence of the B-type fabrics on seismic anisotropy according to the observed
423 shear-wave polarization anisotropy in the northeast Japan.
424 Figure 8 showed variations in the average Vp and deviation of Vp as a function
425 of pressure (P) and temperature (T) for structural planes of varying orientations in P–T
426 space. Pera et al. (2003) presented similar diagrams for A-type olivine fabrics. With
427 respect to the kinematic frameworks of horizontal, lateral, and vertical shear (Fig. 7), Vp
428 shows no significant difference between A-type and B-type olivine fabrics (compare fig.
429 11 in Pera et al., 2003 and Fig. 8A–C of the present study). However, Vs anisotropy
430 shows distinct spatial characteristics: the X direction is the weakest anisotropy for A-type
431 fabrics (fig. 11 in Pera et al., 2003) and the strongest anisotropy for B-type (Fig. 8A–C).
432 These results suggest that for the Imono peridotite body, Vs anisotropy would be
433 similarly weak for any ray path unless the B-type fabrics occur in vertical shear. For the
434 shear along a slab tilted at 30°, Vs anisotropy is sensitive to temperature rather than
435 pressure, although this effect is relatively weak (Fig. 8D).
436 It might be easier to visualize the effect of the kinematic framework on Vs
437 anisotropy by evaluating the thickness (Th) of an anisotropic layer, as given by
438 $$Th=(100dt<Vs>)/AVs,$$

where dt is the delay time of S-waves, <Vs> is the average of the fast and slow velocities, and AVs is the anisotropy for a specific propagation direction expressed as a percentage (Pera et al., 2003; Michibayashi et al., 2006b). We used an average value of S-wave delay time of dt=0.1 s, as reported previously for the fore-arc of northeast Japan (Nakajima and Hasegawa, 2004), and employed the seismic properties of the average Imono olivine CPO shown in Fig. 6.

Figure 10 shows estimates of the thickness of the anisotropic layer in *P*-*T* space. The thickness of the B-type anisotropic layer is only required to be several tens of kilometres thick to satisfy the constraints of S-wave delay time (i.e., dt=0.1 s), regardless of structural orientation in the mantle wedge (Fig. 10). In more detail, where the B-type fabrics occur in the horizontal flow (i.e., the horizontal shear in Fig. 10A or the lateral shear in Fig. 10B), the anisotropic layer would be around 20 km thick. Since the X direction contains the highest anisotropy (Fig. 8C), the anisotropic layer in the vertical shear is only around 10 km thick (Fig. 10C). In the case of shear along a slab tilted at 30°, the thickness of the anisotropic layer varies between 18 km at 800 °C and 16 km at 1000 °C.

Kneller et al. (2005) argued that for B-type fabrics, the thickness of the thermal boundary layer above the slab would be around 10–15 km, where temperature ranges from 700 to 1000 °C. This is largely consistent with our estimate of the thickness of the anisotropic layer (Fig. 10) and the temperature conditions for the B-type fabrics measured in the Imono peridotite body (Fig. 9). Consequently, if the small magnitude of S-wave splitting observed in the fore-arc side of the northeast Japan (Nakajima and Hasegawa, 2004) could be explained by the seismic properties of the B-type peridotites, its anisotropic layer would be approximately several tens of kilometers thick, oriented subparallel to the subducting slab.

In recent studies, the same seismic anisotropy in the Ryukyu arc has been analyzed based on two distinctively different assumptions: the B-type fabric hypothesis (Long et al., 2007; Kneller et al., 2008) and 3D flow caused by foundering of the lower crust (Behn et al., 2007). This debate represents the difficulties involved in interpreting the observed seismic anisotropy. In the present study, although we considered the S-wave anisotropy reported by Nakajima and Hasegawa (2004), the S-wave anisotropy resulted from integration of seismic anisotropy along a near vertical ray path. In contrast, the fast propagation axis of P-waves in the mantle wedge beneath the Tohoku region of northeast

Japan, as inferred from the tomographic inversion of P-waves from local events, is oriented E–W and approximately N–S in the crust and in the Pacific slab that is currently descending beneath the east side of northeast Japan (Ishise and Oda, 2005). The P-wave anisotropy of our B-type fabric would only be compatible with observed N-S anisotropy close to the Pacific slab with structural Y direction parallel to the trench axis and not in the main part of mantle wedge. Nonetheless, we propose that with the identification of B-type fabrics in nature (e.g., Mizukami et al., 2004; Skemer et al., 2006; this study), they should be taken into account when interpreting the present-day seismic anisotropy in the fore-arc side of the mantle wedge (e.g., Audoine et al., 2004), near the slab boundary.

8. Conclusions

B-type olivine fabrics occur pervasively within highly depleted dunites in the small-sized Imono peridotite body located in the subduction-type Sanbagawa metamorphic belt, southwest Japan arc. The dunites contain various microstructures, ranging from porphyroclastic to fine-grained equigranular texture. The Mg numbers of olivine within these dunites are around 0.9, as are the Cr numbers of chromian spinel, suggesting an evolution from highly depleted magma (boninite). Such an origin provides strong thermal constraints on the formation of the highly depleted dunites, which require hot, hydrous, shallow mantle (>1250 °C at <30 km depth) within the mantle wedge. Because the Sanbagawa metamorphic belt entrained these peridotites during progressive retrogression, the B-type olivine fabrics would have developed in the fore-arc side, above or along the subducting slab at maximum temperature conditions of 880–1030 °C depending on the flow stress. The small magnitude of S-wave splitting, orientation of fastest S-wave polarization can be explained by the seismic properties of B-type peridotites within an anisotropic layer of approximately several kilometers in thickness and oriented by flow subparallel to the subducting slab. The B-type layer might therefore represent one of the dominant sources of seismic anisotropy in the fore-arc region.

Acknowledgements

We would like to acknowledge T. Morishita, S. Umino, S. Arai, J. Kimura, and M. Toriumi for their assistance with petrological interpretations, Y. Takei, I. Katayama, T. Hiraga, J. Nakajima, and M. Ishise for their discussions during the course of this project, A. Okamoto for introducing us to the Imono peridotite, and A. Stallard for improving the

505 English of the manuscript. We also acknowledge S. Karato and two anonymous reviewers
506 for their valuable comments and suggestions. MT acknowledges her colleagues, T.
507 Miyake, Y. Omori and M. Muramoto of the Shizuoka University, and K. Kuwatani and W.
508 Nishikanbara of the University of Tokyo for their help in the field and laboratory work
509 and for daily discussions. This study was supported by research grants from the Japan
510 Society for the Promotion of Science (no. 16340151 and 19340148) awarded to KM, the
511 JSPS Invitation Fellowship Programs for Research in Japan (2006) awarded to KM, and
512 the JSPS fellowship (2006) and CNRS/JSPS Exchange Scientist Program in France
513 (2007) awarded to DM.
514
515 References
516 Abramson, E. H., Brown, J. M., Slutsky, L. J., Zang, J. J., 1997. The elastic constants of
517 San Carlos olivine to 17 GPa. J. Geophys. Res. 102, 12,253– 12,263.
518 Arai, S., 1987. An estimation of the least depleted spinel peridotite on the basis of
519 olivine-spinel mantle array. Neues Jahrb. Mineral. Monatsh., 347-354.
520 Arai, S., 1992. Chemistry of chromian spinel in volcanic rocks as a potential guide to
521 magma chemistry. Mineralogical Magazine, 56, 173 – 84.
522 Arai, S., 1994a. Characterization of spinel peridotites by olivine- spinel compositional
523 relationships, review and interpretation. Chemical Geology 113, 191-204.
524 Arai, S., 1994b. Compositional variation of olivine - chromian spinel in Mg-rich magmas
525 as a guide to their residual spinel peridotites. Journal of Volcanology and Geothermal
526 Research 59, 279-294.
527 Aoya, M., 2001. P-T-D path of eclogite from the Sambagawa belt deduced from
528 combination of petrological and microstructural analyses, J. Petrol. 42, 1225–1248.
529 Aoya, M., 2002. Structural position of the Seba eclogite unit in the Sambagawa belt:
530 Supporting evidence for an eclogite nappe. Island Arc 11, 91–110.
531 Audoine, E., Savage, M. K., Gledhill, K., 2004. Anisotropic structure under a back arc
532 spreading region, the Taupo Volcanic Zone, New Zealand. Journal of Geophysical
533 Research 109, B11305, doi:10.1029/2003JB002932.
534 Banno, S., Higashino, T., Otsuki, M., Itaya, T., Nakajima, T., 1978. Thermal structure of
535 the Sambagawa metamorphic belt in central Shikoku, J. Phys. Earth, 26, 345 – 356.
536 Banno, S., Sakai, C., Higashino, T., 1986. Pressuretemperature trajectory of the

537 Sanbagawa metamorphism deduced from garnet zoning, Lithos, 19, 51-63.
538 Behn, M. D., Hirth, G., Kelemen, P. B., 2007. Trench-parallel anisotropy produced by
539 foundering of arc lower crust. Science, 317, 108–111.
540 Conder, J. A., Wiens, D. A., 2007. Rapid mantle flow beneath the Tonga volcanic arc.
541 Earth and Planetary Science Letters, 264, 299–307.
542 Currie, C. A., Cassidy, J. F., Hyndman, R. D., 2001. A regional study of shear wave
543 splitting above the Cascadia subduction zone: Margin-parallel crustal stress.
544 Geophysical Research Letters 28, 659-662.
545 Enami, M., 1982. Oligoclase-biotite zone of the Sanbagawa metamorphic terrain in the
546 Bessi district, central Shikoku, Japan. J. Geol. Soc. Jpn. 88, 887 – 900. (in Japanese
547 with English abstract)
548 Enami, M., Mizukami, T., Yokoyama, K., 2004. Metamorphic evolution of
549 garnet-bearing ultramafic rocks from the Gongen area, Sanbagawa belt, Japan. J.
550 Metamorph. Geol. 22, 1–15.
551 Enami, M., Wallis, S. R., Banno, Y., 1994. Paragenesis of sodic pyroxene-bearing quartz
552 schists: Implications for the P-T history of the Sanbagawa belt. Contrib. Mineral.
553 Petrol., 116, 182–198.
554 Fei Y., 1995. Thermal expansion, in: Ahrens, T. J. (Ed.), Minerals physics and
555 crystallography: a handbook of physical constants, American Geophysical Union,
556 Washington D.C., pp. 29-44.
557 Hacker, B. R., Peacock, S. M., Abers, G. A., Holloway, S. D., 2003. Subduction factory 2.
558 Are intermediate-depth earthquakes in subducting slabs linked to metamorphic
559 dehydration reactions? J. Geophys. Res. 108, 148-227.
560 Hasegawa, A., Umino, N., Takagi, A., 1978. Double-planed structure of the deep seismic
561 zone in the northeastern Japan arc. Tectonophysics 47, 43–58.
562 Higashino, T., 1990. The higher-grade metamorphic zonation of the Sambagawa
563 metamorphic belt in central Shikoku, Japan. J. Metamorph. Geol. 8, 413–423.
564 Horikoshi, G., 1937. On the eclogite in the vicinity of Higashi-akaishi-yama in the
565 province of Iyo. J. Geol. Soc. Jpn. 44, 141–144. (in Japanese)
566 Ishise, M. and Oda, H., 2005. Three-dimensional structure of P-wave anisotropy beneath
567 Tohoku district, northeast Japan. J. Geophys. Res. 110, B07304,
568 doi:10.1029/2004JB003599.
569 Isaak D.G., 1992. High-temperature elasticity of iron-bearing olivine. J. Geophys. Res.

570 97, 1871–1885.
571 Jung, H., Karato, S., 2001a. Water-induced fabric transitions in olivine. Science 293,
572 24-27.
573 Jung, H., Karato, S., 2001b. Effects of water on dynamically recrystallized grain size of
574 olivine. J. Struct. Geol. 23, 1337-1344.
575 Jung, H., Katayama, I., Jiang, Z., Hiraga T., Karato, S., 2006. Effect of water and stress on
576 the lattice-preferred orientation of olivine, Tectonophysics 421, 1 - 22.
577 Karato, S., 1995. Effects of water on seismic wave velocities in the upper mantle.
578 Proceedings of Japan Academy 71, 61-66.
579 Karato, S., 2003. Mapping water content in Earth's upper mantle, in: Eiler, J. E. (Ed.),
580 Inside the Subduction Factory, American Geophysical Union, Washington DC., pp.
581 135-152.
582 Katayama, I., Karato, S., 2006. Effect of temperature on B- to C-type olivine fabric
583 transition and implication for flow pattern in subduction zone. Physics of the Earth and
584 Planetary Interiors 157, 33 - 45.
585 Kelemen., P. B., 1990. Reaction between ultramafic rock and fractionating basaltic
586 magma I. phase reaction, the origin of Calc-alkaline magma series, and the formation
587 of discordant dunite. J. Petrol. 31, 51-98.
588 Kneller, E. A., van Keken, P. E., 2007. Trench-parallel flow and seismic anisotropy in the
589 Mariana and Andean subduction systems. Nature 450, 1222-1225.
590 Kneller, E. A., van Keken, P. E., Katayama, I., Karato, S., 2007. Stress, strain, and B-type
591 olivine fabric in the fore-arc mantle: Sensitivity tests using high-resolution steady-state
592 subduction zone models. J. Geophys. Res. 112, B04406, doi:10.1029 /2006JB004544.
593 Kneller, E. A., P. E. van Keken., S. Karato., J. Park, 2005. B-type olivine fabric in the
594 mantle wedge: Insights from high-resolution non-Newtonian subduction zone models.
595 Earth and Planetary Science Letters 237, 781 - 797.
596 Kneller, E. A., Long, M. D., van Keken, P. E., 2008. Olivine fabric transitions and shear
597 wave anisotropy in the Ryukyu subduction system. Earth and Planetary Science Letters
598 268, 268-282.
599 Knittle, E., 1995. Static compression measurements of equation of state, in: Ahrens, T. J.
600 (Ed.), Minerals physics and crystallography: a handbook of physical constants,
601 American Geophysical Union, Washington D.C., pp. 98-142.
602 Kunugiza, K., 1984. Metamorphism and origin of ultramafic bodies of the Sanbagawa

603 metamorphic belt in central Shikoku. J. Jpn. Assoc. Min. Petrol. Econ. Geol. 79, 20 –
604 32. (in Japanese with English abstract)
605 Kunugiza, K., Takasu, A., Banno, S., 1986. The origin and metamorphic history of the
606 ultramafic and metagabbro bodies in the Sanbagawa belt. Geol. Soc. Am. Mem. 164,
607 375 – 385.
608 Lassak, T. M., Fouch, M. J., Hall, C. E., Kaminski, E., 2006. Seismic characterization of
609 mantle flow in subduction systems: Can we resolve a hydrated mantle wedge? Earth
610 and Planetary Science Letters 243, 632-649.
611 Long, M. D., Hager, B. H., de Hoop, M. V., van der Hilst, R. D., 2007. Two-dimensional
612 modeling of subduction zone anisotropy with application to southwestern Japan.
613 Geophys. J. Int. 170, 839-856.
614 Mainprice, D., 2007. Seismic anisotropy of the deep Earth from a mineral and rock
615 physics perspective. In: Schubert, G., (Ed.), Treatise on Geophysics volume **2**, Oxford,
616 Elsevier Ltd., pp. 437-492.
617 Mainprice, D., Barruol, G., Ben Ismaïl, W., 2000. The anisotropy of the Earth's mantle:
618 from single crystal to polycrystal, in: S. Karato, A.M. Forte, R.C. Liebermann, G.
619 Masters, L. Stixrude (Eds.), Mineral Physics and Seismic Tomography: From Atomic
620 to Global, AGU Geophysical Monograph, vol. 117, pp. 237–264.
621 Maruyama, S., Isozaki, Y., Kimura, G., Terabayashi, M., 1997. Paleogeographic maps of
622 the Japanese islands: plate tectonic synthesis from 750 Ma to the present. The Island
623 Arc 6, 121-142.
624 Michibayashi, K., 1993. Syntectonic development of a strain independent dynamically
625 recrystallized quartz grain during mylonitization. Tectonophysics 222, 151-164.
626 Michibayashi, K., Mainprice, D., 2004. The role of pre-existing mechanical anisotropy
627 on shear zone development within oceanic mantle lithosphere: an example from the
628 Oman ophiolite. J. Petrol. 45, 405–414.
629 Michibayashi, K., Masuda, T., 1993. Shearing during progressive retrogression in
630 granitoids: abrupt grain size reduction of quartz at the plastic-brittle transition for
631 feldspar. J. Struct. Geol. 15, 1421-1432.
632 Michibayashi, K., Ina, T., Kanagawa, K., 2006a. The effect of dynamic recrystallization
633 on olivine fabric and seismic anisotropy: Insight from a ductile shear zone, Oman
634 ophiolite, Earth and Planetary Science Letters 244, 695–708.
635 Michibayashi, K., Abe, N., Okamoto, A., Satsukawa, T., Michikura, K., 2006b. Seismic

636 anisotropy in the uppermost mantle, back-arc region of the northeast Japan arc:
637 Petrophysical analyses of Ichinomegata peridotite xenoliths, Geophysical Research
638 Letters 33, doi:10.1029/2006GL025812.
639 Mizukami, T., Wallis, S. R., 2005. Structural and petrological constraints on the tectonic
640 evolution of the garnet-lherzolite facies Higashi-akaishi peridotite body, Sanbagawa
641 belt, SW Japan. Tectonics 24, 1 - 17.
642 Mizukami, T., Wallis, S. R., Yamamoto, J., 2004. Natural example of olivine lattice
643 preferred orientation patterns with a flow-nomal a-axis maximum. Nature 427, 29-32.
644 Mori, T., Banno, S., 1973. Petrology of peridotite and garnet clinopyroxenite of the Mt.
645 Higashi- Akaishi mass, Central Shikoku, Japan: Subsolidus relation of anhydrous
646 phases. Contrib. Mineral. Petrol. 41, 301 – 323.
647 Nakajima, J., Hasegawa, A., 2004. Shear-wave polarization anisotropy and
648 subduction-induced flow in the mantle wedge of northeastern Japan. Earth and
649 Planetary Science Letters 225, 365– 377.
650 Nicolas, A., Christensen, N.I., 1987. Formation of anisotropy in upper mantle peridotite:
651 a review, in: K. Fuchs, C. Froidevaux (Eds.), Composition Structure and Dynamics of
652 the Lithosphere–Asthenosphere System, Geodyn. Monogr. Ser., AGU, Washington, D.
653 C., 111 - 123.
654 Okamoto, A., Michibayashi, K., 2005. Progressive shape evolution of a mineral inclusion
655 under differential stress at high temperature: example of garnet inclusions within a
656 granulite facies from the Lutow-Holm complex, East Antarctica. Journal of
657 Geophysical Research 110, B11203, doi:10.1029/2004JB003526.
658 Okamoto, K., Maruyama, S., Isozaki, Y., 2000. Accretionary complex origin of the
659 Sanbagawa, high P/T metamorphic rocks, central Shikoku, Japan – Layer-parallel
660 shortening structure and green stone geochemistry. J. Geol. Soc. Jpn. 106, 70 – 86.
661 Pera, E., Mainprice, D., Burlinic, L., 2003. Anisotropic seismic properties of the upper
662 mantle beneath the Torre Alfina area (Northern Apennines, Central Italy).
663 Tectonophysics 370, 11-30.
664 Peyton, V., Levin, V., Park, J., Brandon, M., Lees, J., Gordeev, E., Ozerov, A., 2001.
665 Mantle flow at a slab edge: seismic anisotropy in the Kamchatka region. Geophysical
666 Research Letters 28, 379-382.
667 Skemer, P., Katayama, I., Karato, S., 2006. Deformation fabrics of the Cima di Gagnone
668 peridotite massif, Central Alps, Switzerland: evidence of deformation at low

669 temperatures in the presence of water. Contri. Mineral. Petrol. 152, 43 - 51.
670 Smith, P. G., Wiens, D. A., Fischers, K. M., Dorman, L. M., Webb, S. C., Hildebrand, J. A.,
671 2001. A complex pattern of mantle flow in the Lau backarc. Science 292, 713-716.
672 Stöckert, B., Gerya, T. V., 2005. "Pre-collisional HP metamorphism and nappe tectonics
673 at active continental margins: a numerical simulation." Terra Nova
674 doi10.1111/j.1365-3112.2004.00589.
675 Takahashi, E., Tro, K., Schilling, J. G., 1987. Primary magma compositions and Mg/Fe
676 ratios of their mantle residues along Mid Atlantic Ridge 29°N to 73°N. Technical
677 Reports ISEI, Okayama Univeircity, 1-4.
678 Takasu, A., 1989. P-T histories of peridotite and amphibolite tectonic blocks in the
679 Sanbagawa metamorphic belt, Japan, in: Daly, J. S., Cliff, R. A., Yardley, B. W. D.
680 (Eds.), Evolution in Metamorphic Belts, Spec. Publ. Geol. Soc., 43, pp.533–536.
681 Takasu, A., Dallmeyer, R. D., 1990. 40Ar/39Ar mineral age constraints for the
682 tectonothermal evolution of the Sambagawa metamorphic belt, central Shikoku, Japan:
683 A Cretaceous accretionary prism. Tectonophysics 185, 111 – 139.
684 Tatsumi, Y., 1989. Migration of fluid phases and genesis of basalt magmas in subduction
685 zones. J. Geophys. Res. 94, 4697 – 4707.
686 Twiss, R. J., 1977. Theory and applicability of a recrystallized grain size paleopiezometer.
687 Pure. Appl. Geophys. 115, 227-244.
688 Umino, S., Kushiro, I., 1989. Experimental Studies on boninite petrogenesis, In:
689 Crawford, A. J. (Ed.), Boninite and Related Rocks, Unwin Hyman, London, pp.
690 89-111.
691 Van der Wal, D., Chopra, P., Drury, M. R., Fitzgerald, J. D., 1993. Relationships between
692 dynamically recrystallized grain size and deformation conditions in experimentally
693 deformed olivine rocks. Geophysical Research Letters 20, 1479-1482.
694 Wallis, S. R., 1995. Exhuming the Sanbagawa belt: The importance of tectonic
695 discontinuities. J. Metamorph. Geol. 16, 83 – 95.
696 Wallis, S. R., Aoya, M., 2000. A re-evaluation of eclogite facies metamorphism in SW
697 Japan: Proposal for an eclogite nappe. J. Metamorph. Geol. 18, 653 – 664.
698 Wallis, S. R., Takasu, A. Enami, M., Tsujimori, T., 2000. Eclogite and related
699 metamorphism in the Sanbagawa Belt, southwest Japan. Bull. Res. Inst. Nat. Sci.
700 Okayama Univ. Sci. 26, 3 – 17.

701 Yamamoto, H., Okamoto, K., Kaneko, Y., Terabayashi, M., 2004. Southward extrusion
702 of eclogite-bearing mafic–ultramafic bodies in the Sanbagawa belt, central Shikoku,
703 Japan. Tectonophysics 387, 151– 168.
704 Yoshino, G., 1961. Structural-petrological studies of peridotite and associated rocks of the
705 Higashiakaishi- yama district, Shikoku, Japan. J. Sci. Hiroshima Univ., Ser. C 3, 343 –
706 402.
707 Yoshino, G., 1964. Ultrabasic mass in the Higashiakaishiyama district, Shikoku, Japan. J.
708 Sci. Hiroshima Univ., Ser. C 4, 333 – 364.
709

710 Figure captions
711
712 Fig. 1. (A) Geological map of the Besshi area (modified after Aoya, 2001). The Imono
713 peridotite body is located 5 km east of Mt. Higashi-Akaishi (HA). IRT: Iratsu mafic body.
714 (B) Enlargement of the Imono peridotite body, showing the location of the sampled
715 outcrop (N08) on the eastern side of the body and the orientation of foliation and
716 lineation.
717
718 Fig. 2. Photomicrographs of Imono peridotites, showing porphyroclastic textures (A–D)
719 and fine-grained equigranular textures (E and F). Scale bars are all 1 mm. The proportion
720 of neoblasts varies among the samples with porphyroclastic textures (A–D).
721
722 Fig. 3. Olivine CPO data. Equal area, lower hemisphere projections. Contours are
723 multiples of uniform distribution. Foliation is horizontal and lineation is E–W. The labels
724 correspond to those in Fig. 2; whreas C represents all olivine grains, C1 and C2 represent
725 porphyroclasts and neoblasts within C, respectively. *J*, *M* and *pfJ* are the fabric intensities
726 calculated after Mainprice et al. (2000), Michibayashi and Mainprice (2004) and Skemer
727 et al. (2006).
728
729 Fig. 4. (A) Relationships between the Mg number of olivine and the Cr/(Cr+Al) atomic
730 ratio (=Cr#) of chromian spinel in analysed samples. OSMA: olivine–spinel mantle array.
731 (B) Relationships between the Mg number and Ni content of olivine in analysed samples.
732 (C) Relationships between the Ti content and the Cr/(Cr+Al) atomic ratio (=Cr#) of
733 chromian spinel in analysed samples.
734
735 Fig. 5. Seismic properties computed from the CPO of olivine within analyzed samples.
736 Each panel corresponds to the same sample shown in the same panel in Fig. 2. Data are
737 presented in an equal area lower hemisphere projection. Foliation is horizontal (XY
738 plane; solid line) and lineation (X) is E-W within the plane of the foliation. Column 1
739 (Vp): 3D distribution of the P-wave velocity. Contours are multiples of the uniform
740 density. Anisotropy is VpMax-VpMin/VpMean. Column 2 (AVs): 3D distribution of the
741 polarization anisotropy of S-waves owing to S-wave splitting. Column 3 (Vs_1 plane):
742 polarization plane of the fast split S-wave (S_1) as a function of the orientation of the

743 incoming wave relative to the structural frame (X, Y, Z) of the sample. Each small
744 segment on the figure represents the trace of the polarization plane on the point at which
745 S_1 penetrates the hemisphere. Color shading for AVs is also shown on the figure.
746
747 Fig. 6. (A) Olivine CPO pattern and (B) seismic properties of the Imono average sample.
748 Contours are multiples of uniform density. Foliation is horizontal (XY plane; solid line),
749 and the lineation (X) is oriented E–W within the plane of the foliation. See Figure 5
750 caption.
751
752 Fig. 7. Different structural orientations of mantle peridotite. Shaded area: foliation plane;
753 lines: lineation directions. (A) horizontal shear model; (B) lateral shear model; (C)
754 vertical shear model; (D) a model of shear along a slab tilted 30 degree. (E) The
755 relationships between the propagation directions of seismic waves and four shear models.
756 The four shear models correspond to different parts of the corner flow in the mantle
757 wedge.
758
759 Fig. 8. Variations in average Vp, deviation of Vp and S-wave anisotropy as a function of
760 *P* and *T* for the Imono average sample with respect to the different structural orientations
761 shown in Fig. 7. Seismic properties were calculated using the elastic constants of
762 Abramson et al. (1997), pressure and temperature derivatives of Abramson et al. (1997)
763 and Isaak (1992), respectively, and the Voigt-Reuss-Hill average. The *PT* conditions for
764 the B-type olivine fabrics of the Imono peridotites are indicated by dotted triangles.
765
766 Fig. 9. Possible *P*-*T* conditions of the Imono peridotite body in comparison with the
767 P-T-D path of the Higashi-Akaishi peridotite body, as proposed by Mizuoka and Wallis
768 (2005), as well as the *P*-*T* path of the Sanbagawa metamorphic body. Two inferred
769 maximum temperature conditions for the B-type fabrics are shown with respect to two
770 flow stresses: 880 °C for 100 MPa and 1030 °C for 200 MPa, respectively. See text for
771 discussion.
772
773 Fig. 10. Estimate of the thickness of the anisotropic layer. Based on the observed dt=0.1 s,
774 we have an anisotropic layer with a thickness of several tens of kilometers, regardless of
775 the structural orientation of B-type olivine fabrics within the Imono peridotite body.

Figure

Click here to download Figure: Tasaka_etal_Figures.doc

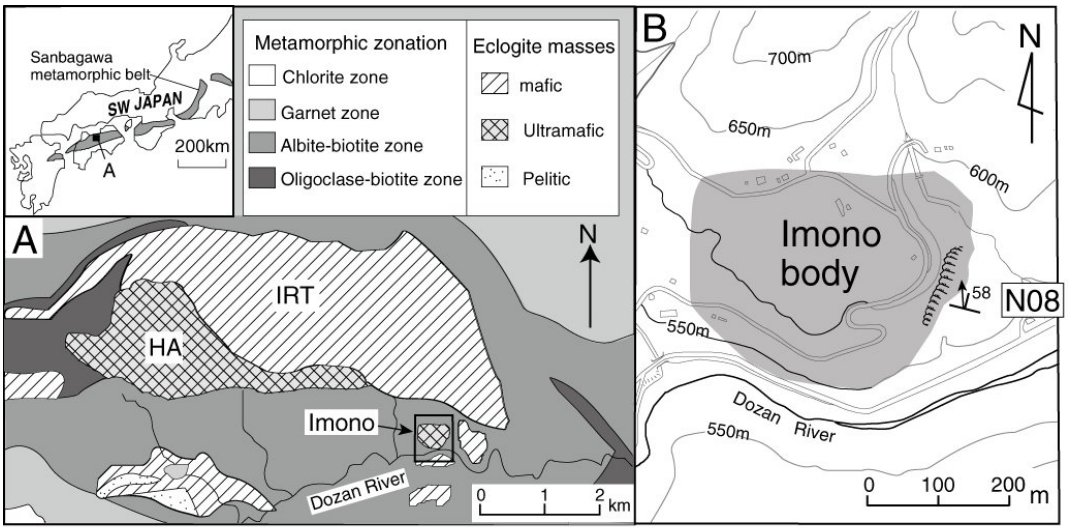

Fig. 1. (A) Geological map of the Besshi area (modified after Aoya, 2001). The Imono peridotite body is located 5 km east of Mt. Higashi-Akaishi (HA). IRT: Iratsu mafic body. (B) Enlargement of the Imono peridotite body, showing the location of the sampled outcrop (N08) on the eastern side of the body and the orientation of foliation and lineation.

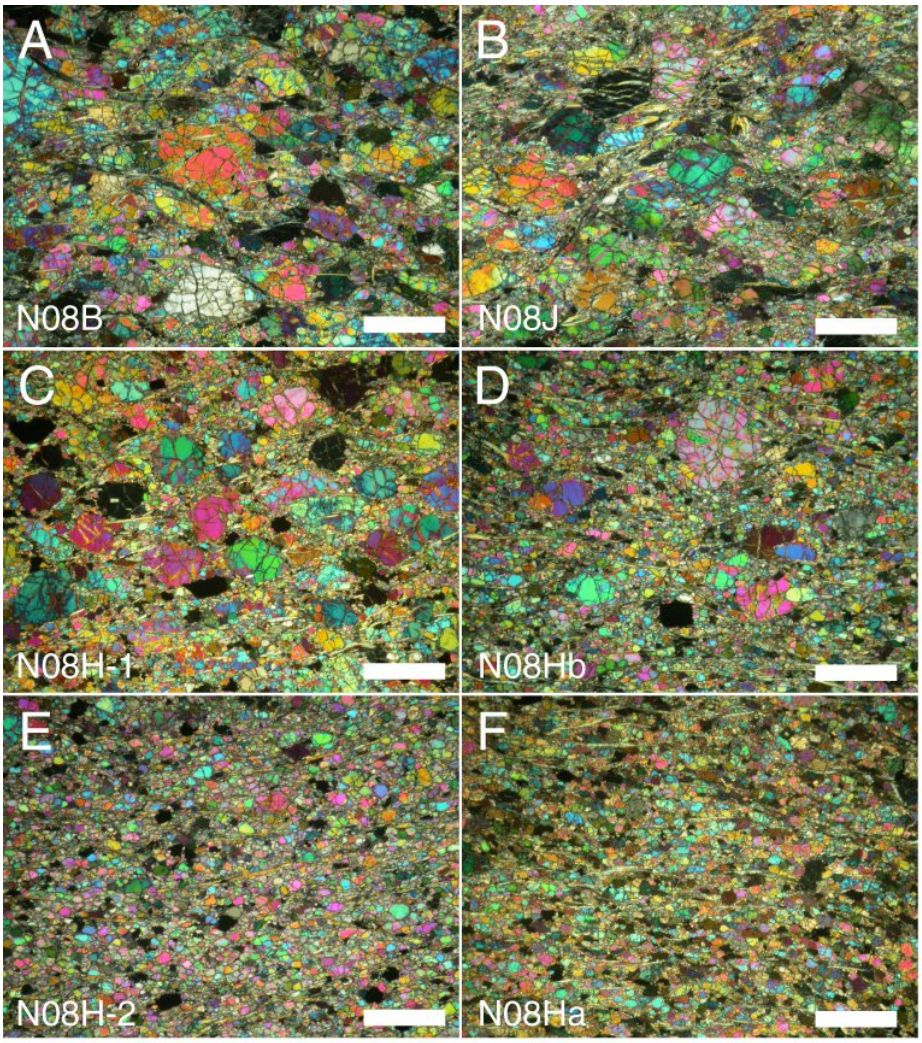

Fig. 2. Photomicrographs of Imono peridotites, showing porphyroclastic textures (A–D) and fine-grained equigranular textures (E and F). Scale bars are all 1 mm. The proportion of neoblasts varies among the samples with porphyroclastic textures (A–D).

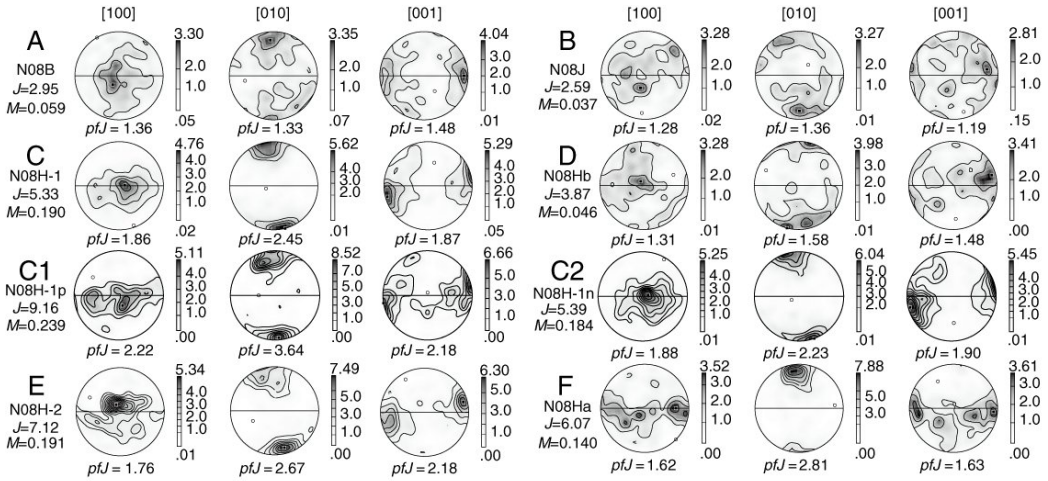

Fig. 3. Olivine CPO data. Equal area, lower hemisphere projections. Contours are multiples of uniform distribution. Foliation is horizontal and lineation is E–W. The labels correspond to those in Fig. 2; whreas C represents all olivine grains, C1 and C2 represent porphyroclasts and neoblasts within C, respectively. *J*, *M* and *pfJ* are the fabric intensities calculated after Mainprice et al. (2000), Michibayashi and Mainprice (2004) and Skemer et al. (2006).

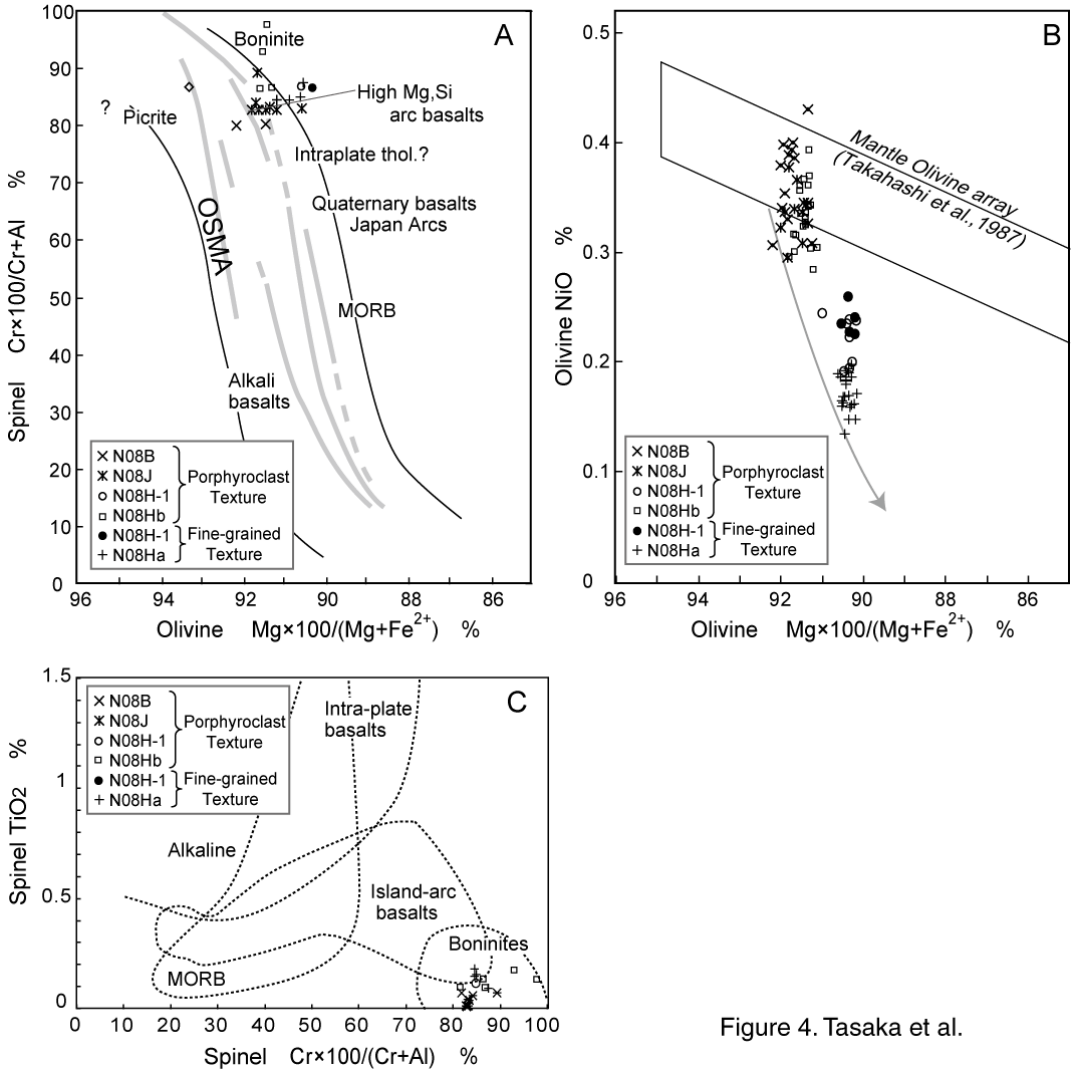

Figure 4. Tasaka et al.

Fig. 4. (A) Relationships between the Mg number of olivine and the Cr/(Cr+Al) atomic ratio (=Cr#) of chromian spinel. OSMA: olivine-spinel mantle array. (B) Relationships between the Mg number and Ni content of olivine. (C) Relationships between the Ti content and the Cr/(Cr+Al) atomic ratio (=Cr#) of chromian spinel,

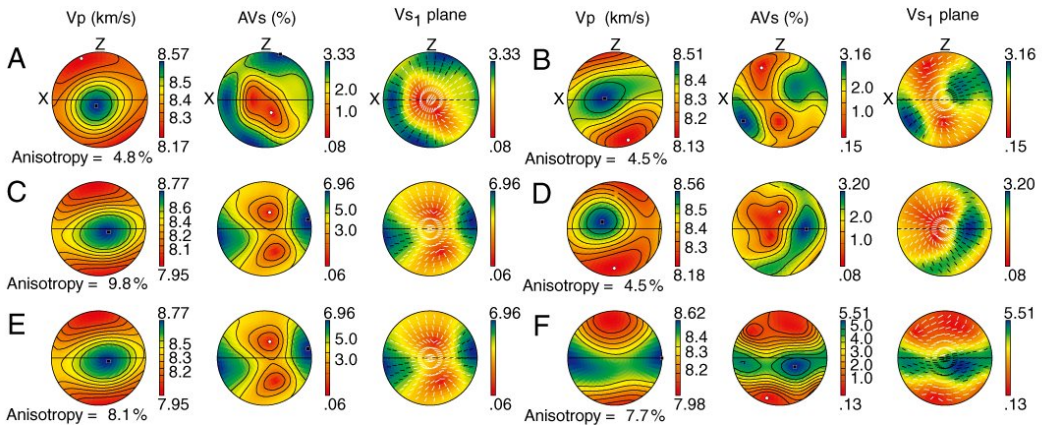

Fig. 5. Seismic properties computed from the CPO of olivine within analyzed samples. Each panel corresponds to the same sample shown in the same panel in Fig. 2. Data are presented in an equal area lower hemisphere projection. Foliation is horizontal (XY plane; solid line) and lineation (X) is E-W within the plane of the foliation. Column 1 (Vp): 3D distribution of the P-wave velocity. Contours are multiples of the uniform density. Anisotropy is VpMax-VpMin/VpMean. Column 2 (AVs): 3D distribution of the polarization anisotropy of S-waves owing to S-wave splitting. Column 3 (Vs_1 plane): polarization plane of the fast split S-wave (S_1) as a function of the orientation of the incoming wave relative to the structural frame (X, Y, Z) of the sample. Each small segment on the figure represents the trace of the polarization plane on the point at which S_1 penetrates the hemisphere. Color shading for AVs is also shown on the figure.

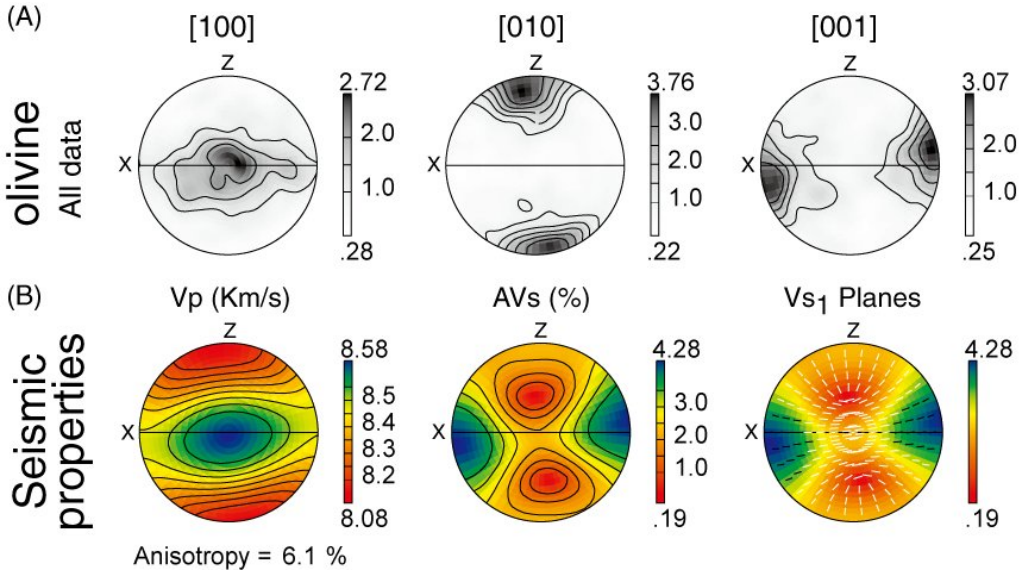

Fig. 6. (A) Olivine CPO pattern and (B) seismic properties of the Imono average sample. Contours are multiples of uniform density. Foliation is horizontal (XY plane; solid line), and the lineation (X) is oriented E–W within the plane of the foliation. See Figure 5 caption.

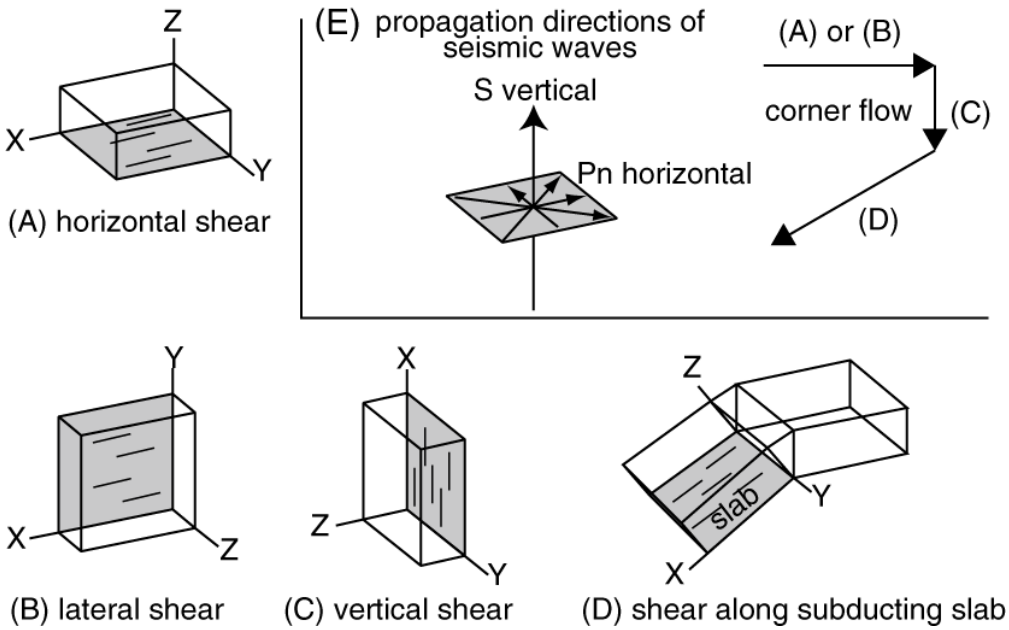

Fig. 7. Different structural orientations of mantle peridotite. Shaded area: foliation plane; lines: lineation directions. (A) horizontal shear model; (B) lateral shear model; (C) vertical shear model; (D) a model of shear along a slab tilted 30 degree. (E) The relationships between the propagation directions of seismic waves and four shear models. The four shear models correspond to different parts of the corner flow in the mantle wedge.

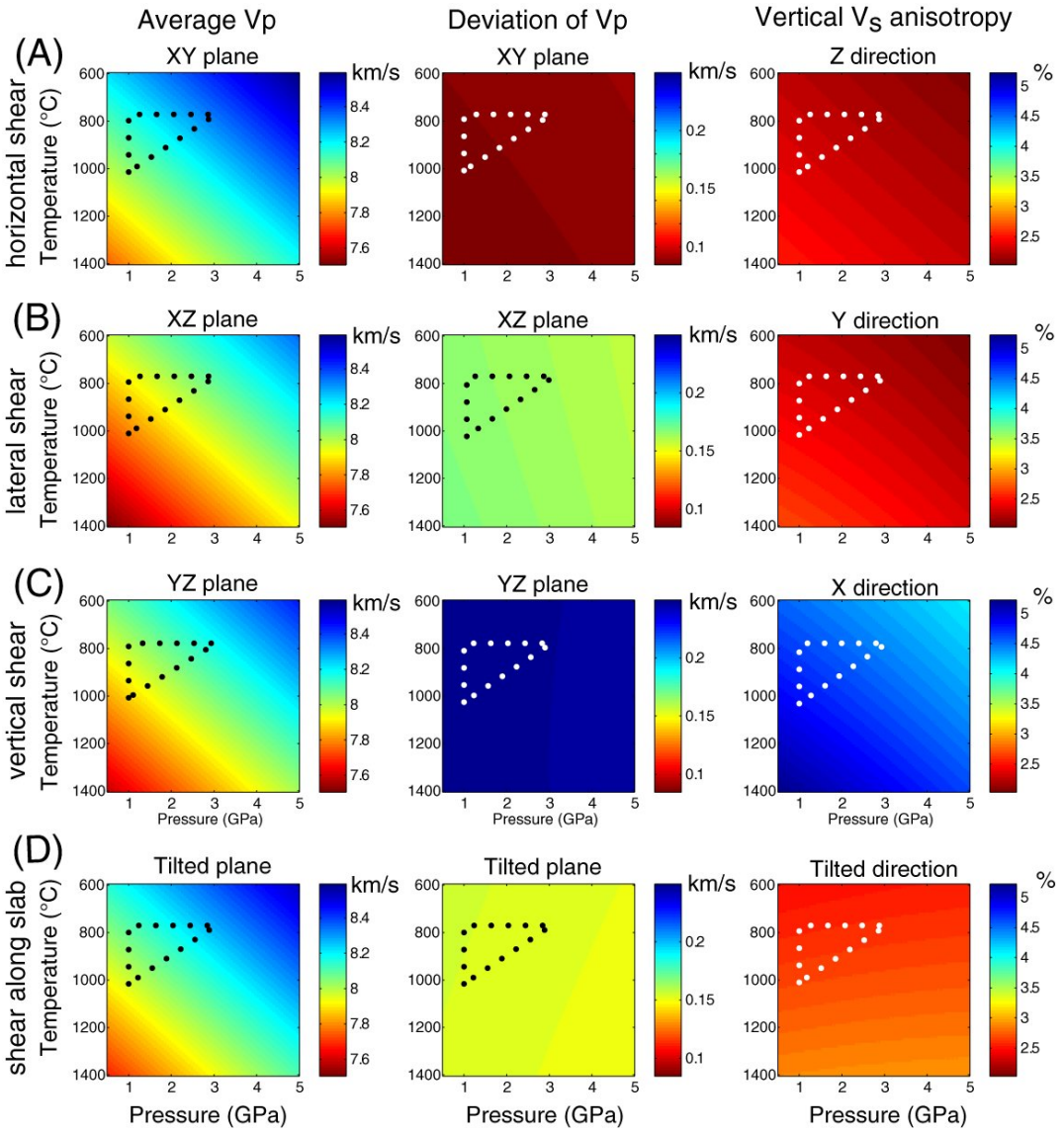

Fig. 8. Variations in average Vp, deviation of Vp and S-wave anisotropy as a function of *P* and *T* for the Imono average sample with respect to the different structural orientations shown in Fig. 7. Seismic properties were calculated using the elastic constants of Abramson et al. (1997), pressure and temperature derivatives of Abramson et al. (1997) and Isaak (1992), respectively, and the Voigt-Reuss-Hill average. The *PT* conditions for the B-type olivine fabrics of the Imono peridotites are indicated by dotted triangles.

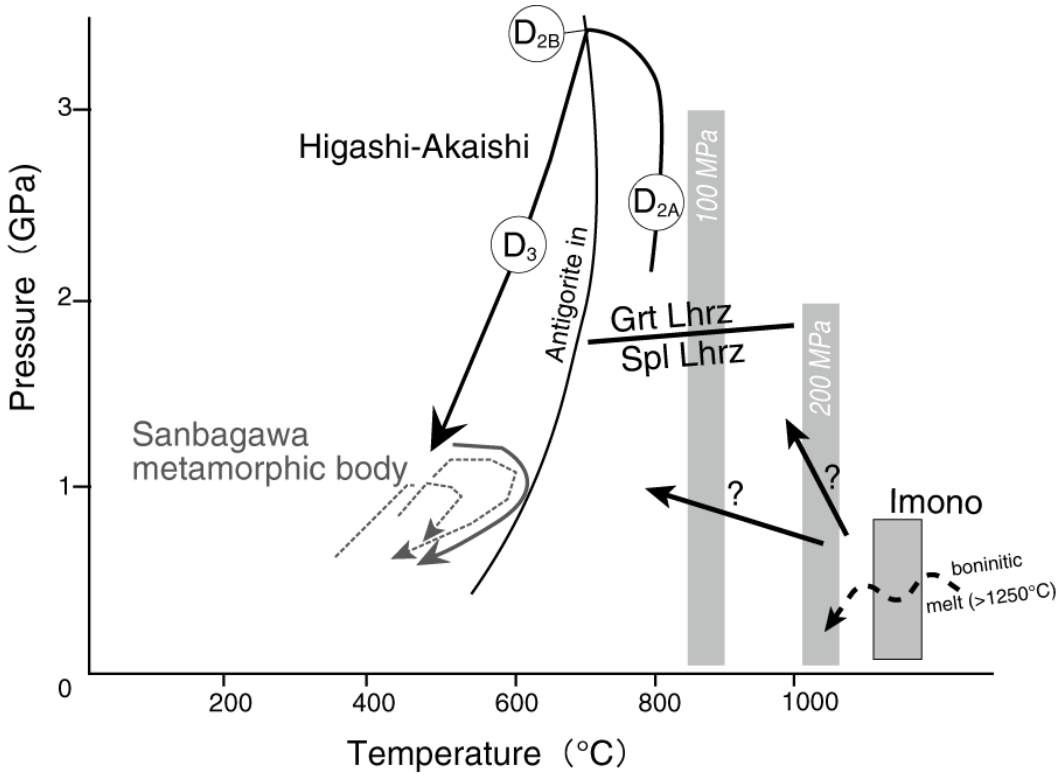

Figure 9. Tasaka et al.

Fig. 9. Possible P-T conditions of the Imono peridotite body in comparison with the P-T-D path of the Higashi-Akaishi peridotite body, as proposed by Mizuoka and Wallis (2005), as well as the P-T path of the Sanbagawa metamorphic body. Two inferred maximum temperature conditions for the B-type fabrics are shown with respect to two flow stresses: 880 °C for 100 MPa and 1030 °C for 200 MPa, respectively. See text for discussion.

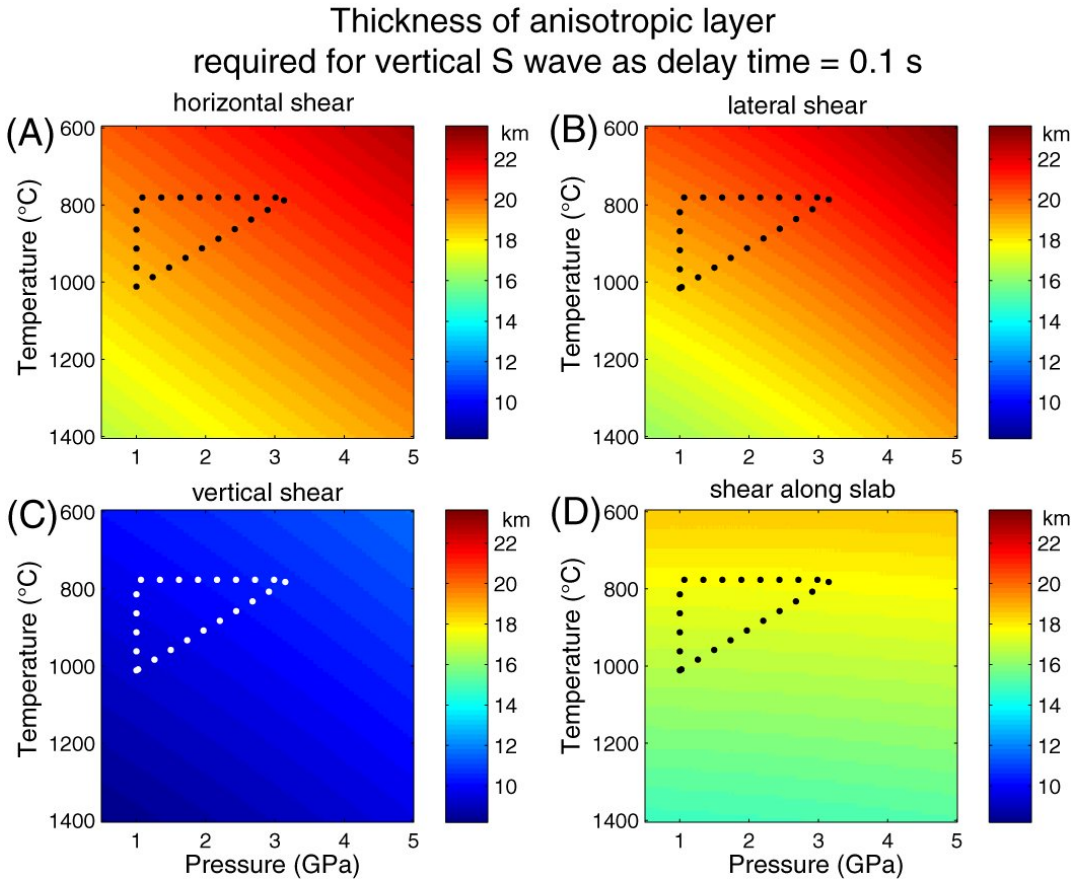

Fig. 10. Estimate of the thickness of the anisotropic layer. Based on the observed dt=0.1 s, we have an anisotropic layer with a thickness of several tens of kilometers, regardless of the structural orientation of B-type olivine fabrics within the Imono peridotite body.